Research Square

Preprints are preliminary reports that have not undergone peer review.
They should not be considered conclusive, used to inform clinical practice,
or referenced by the media as validated information.

Electronic Tuning of Dynamic Imine Bonds Enables Programmable Pore Gating in Metal–Organic Frameworks

Shuai Yuan

syuan@nju.edu.cn

Nanjing University https://orcid.org/0000-0003-3329-0481

Meng Qiao

China Pharmaceutical University

Youcong Li

Nanjing University

Shengcun Chen

Nanjing Normal University

Sirui Liu

Nanjing Normal University

Yu-Hao Gu

Nanjing University https://orcid.org/0009-0008-9141-2495

Dong Zhang

Nanjing University

Yi-Fan Liu

Nanjing University

Lei Gao

Nanjing University https://orcid.org/0009-0005-8449-4208

Mengting Chang

Nanjing Normal University

Xing Zhang

Nanjing Normal University

Article

Keywords:

Posted Date: May 11th, 2026

DOI: https://doi.org/10.21203/rs.3.rs-9376519/v1

License: This work is licensed under a Creative Commons Attribution 4.0 International License.
Read Full License

Additional Declarations: There is **NO** Competing Interest.

Version of Record: A version of this preprint was published at Nature Communications on October 15th, 2026. See the published version at https://doi.org/10.1038/s41467-026-78657-9.

Abstract

Metal–organic frameworks (MOFs) are promising host matrices for molecular encapsulation, yet their application is often limited by fixed pore apertures that exclude guest molecules larger than the pore openings. Herein, we overcome this limitation by electronic tuning of dynamic imine bonds to induce reversible pore gating that transiently expands framework accessibility beyond its intrinsic aperture. By incorporating imine-based linkers bearing electron-donating/withdrawing substituents into a robust Zr-based MOF scaffold via postsynthetic linker exchange, we systematically modulate imine dissociation equilibria while preserving crystallinity. A linear correlation between Hammett substituent constants and imine bond stability establishes electronic effects as a predictive handle for programming framework dynamics. Systematic variation of substituents establishes an optimal metastable regime in which reversible linker dissociation permits size-adaptive guest uptake without structural degradation. As a proof of concept, paclitaxel and other therapeutics are efficiently encapsulated, and the resulting materials exhibit excellent biocompatibility together with programmable, environment-responsive release kinetics under physiological conditions.

Introduction

Metal–organic frameworks (MOFs) provide highly tunable porous platforms for molecular encapsulation, enabling precise control over host-guest interactions[1–7]. Their high surface areas, structural tunability, and well-defined pore architectures have led to widespread applications in gas storage[8–15], drug delivery[16–22], and enzyme immobilization[23–25]. Guest incorporation into MOFs is generally achieved through either in situ encapsulation during synthesis or postsynthetic adsorption. While in situ encapsulation enables the incorporation of large species during framework growth, it requires synthesis conditions compatible with the guests, thereby severely restricting MOF selection and limiting its general applicability[25–27]. Conversely, postsynthetic adsorption allows guest immobilization into a broad range of preformed frameworks under mild conditions[28–32], but it is inherently constrained by size exclusion, as guest molecules larger than the pore apertures of MOFs cannot access the internal cavities even if pore volume is sufficient.

To address pore aperture limitations, various defect engineering strategies have been implemented to expand MOF pore sizes. Early studies demonstrated that the modulated synthesis of zirconium-based MOFs, such as UiO-66, using monocarboxylic acid modulators can deliberately introduce structural defects, thereby increasing the accessible porosity[33]. Subsequently, Zhou and coworkers developed linker labilization, where imine-based labile linkers are selectively removed to allow programmed defect formation and pore size enlargement[34]. This concept was later extended to other cleavable linkages, including the thermolysis of carboxylate linkers[35] and ozonolysis of alkene-functionalized linkers[36]. Recently, we demonstrated that the hydrolysis of B–O bond-based linkers can induce controlled bond cleavage and pore expansion, thereby enabling the encapsulation of enzymes larger than the native pore size[37]. Despite their effectiveness, these approaches rely on permanent defect formation. Excessive

defect generation may undermine framework stability, whereas enlarged apertures can increase the risk of guest leakage, highlighting the intrinsic trade-off between pore accessibility and structural integrity.

Beyond defect engineering, the dynamic behavior of frameworks provides an alternative strategy for overcoming aperture constraints[38–40]. Instead of permanently enlarging pores, reversible bond dissociation can temporarily open the aperture, allowing guest molecules larger than the intrinsic pore windows to infiltrate while preserving framework integrity. For example, Tsung and coworkers developed an aperture-opening approach through dissociative linker exchange in UiO-66 hosts under controlled solvent conditions, achieving efficient guest encapsulation[41]. In our previous work, reversible metal–pyridyl coordination was employed to create dynamic coordination gates that transiently opened transport pathways, enabling enzymes larger than the native pore windows to penetrate MOF particles[42]. More recently, a dynamic exchange strategy based on reversible imine linkages in COF single-crystals was shown to mediate enzyme incorporation through bond reconfiguration, thereby bypassing intrinsic pore size constraints without permanent defect creation or aperture enlargement[43]. These studies highlight the potential of exploiting reversible bond dynamics in framework materials to enable size-adaptive guest uptake. However, current systems largely rely on intrinsic bond lability and lack a predictive method to balance the framework stability and dynamics.

Herein, we report a strategy to program pore gating in MOFs through electronic tuning of dynamic imine bonds. By incorporating imine-based linkers bearing electron-donating or electron-withdrawing substituents into a robust Zr-based scaffold via postsynthetic exchange, we established a linear correlation between Hammett substituent constants and imine dissociation equilibria (Fig. 1a). This electronic modulation of functional groups generates a tunable metastable window in which reversible linker dissociation induces programmable pore gating without structural collapse. The resulting dynamic equilibrium enables size-adaptive guest uptake beyond intrinsic aperture limitations while preserving crystallinity. The utility of this method was further demonstrated by the loading and delivery of therapeutics, including paclitaxel, epirubicin, and genistein, where the resulting materials exhibited excellent biocompatibility and programmable drug release behavior under physiological conditions in vitro (Fig. 1b). This work introduces electronic tuning as a predictive design principle for programming framework metastability and dynamics, providing a generalizable pathway toward adaptive porous materials.

Results and Discussion

Construction of imine-linked MOFs with substituent variation

To establish a platform for programmable framework dynamics, we selected Zr-based PCN-160 as the parent scaffold because of its exceptional chemical stability and its amenability to postsynthetic functionalization via linker exchange[34,44]. The original robust azobenzene-4,4’-dicarboxylate (AZDC)

linker was replaced with hydrolytically labile imine-based linkers. This design enables the incorporation of dynamic covalent motifs while retaining the robust Zr–carboxylate backbone, thereby decoupling structural integrity from dynamic functionality. To systematically modulate the stability of the imine linkage, a series of substituted imine linkers bearing electron-donating (e.g., $–CH_3$) and electron-withdrawing (e.g., –F, –Cl) groups was designed (Supplementary Table S1). Substituents were introduced at different positions on the aromatic rings to generate controlled electronic perturbations (Fig. 2a). Because imine bond strength is sensitive to the electronic distribution across the C = N moiety, such substitutions are expected to alter imine dissociation equilibria, thereby tuning framework stability and dynamic behavior without modifying framework topology or pore geometry.

Direct solvothermal synthesis of imine-based PCN-160 derivatives is not successful, as imine linkers are unstable under harsh solvothermal synthetic conditions. Therefore, the dynamic linkers were incorporated via postsynthetic linker exchange of preformed PCN-160 single crystals. The resulting materials are denoted as PCN-160-X (X = 1–10), where X corresponds to imine linkers bearing different substituents. Single crystals of all the PCN-160-X (X = 1–10) derivatives were successfully obtained, providing direct structural evidence of successful linker exchange. All PCN-160-X derivatives crystallize in the cubic space group *Fm-3m* (Supplementary Tables S2-S4), identical to pristine PCN-160. Compared with pristine PCN-160 containing azobenzene linkers (a = b = c = 29.39 Å), the imine-based PCN-160-X derivatives exhibit slightly expanded unit cell parameters (a = b = c = 29.49–29.67 Å), which can be attributed to the longer imine bond length and the presence of bulky substituent groups. The overall framework structure remains unchanged after linker exchange. In PCN-160-X, each Zr_6-cluster is coordinated by twelve dicarboxylate linkers to form a UiO-type framework with face-centered cubic topology. The $–CH_3$, –F, and –Cl functional groups are clearly resolved in the refined crystal structures, confirming successful linker incorporation. The exchange process was visually evident from the color change of the crystals from red to pale yellow (Fig. S1), indicating the replacement of azobenzene moieties with imine linkers. Optical microscopy and single-crystal X-ray diffraction confirm that the transformation proceeds via a single-crystal-to-single-crystal pathway rather than dissolution-recrystallization, as the crystal size and morphology are retained (Fig. 2b).

Powder X-ray diffraction (PXRD) analysis confirmed the bulk purity of the PCN-160 derivatives, with patterns closely matching those of the parent PCN-160 (Fig. 2b). The proton nuclear magnetic resonance (^{1}H NMR) spectra of the digested samples confirm the quantitative replacement of the azobenzene linker by imine linkers (Figs. S2-S11). Infrared (IR) spectra provide additional confirmation, the emergence of characteristic substituent bands, including Ar–F (1237 cm^{-1}), Ar–Cl (1053 cm^{-1}), and C–H (437 cm^{-1}) peaks from imine moieties, verified successful linker exchange (Fig. 2c). Transmission electron microscopy (TEM) revealed that the crystal morphology and size are preserved after linker exchange (Figs. 2e-f). Elemental mapping by energy dispersive spectroscopy (EDS) under TEM revealed a uniform distribution of C, N, O, Zr, and F throughout the crystals of the substituted PCN-160-2, further confirming complete linker exchange rather than surface modification (Figs. 2f, S12-18). Thermogravimetric analysis (TGA) curves revealed similar weight loss at ~ 500°C, corresponding to the

decomposition of organic linkers. The comparable weight loss across the series indicates a consistent metal-to-linker ratio, suggesting the preservation of defect-free frameworks after postsynthetic modification (Fig. S19).

The porosity of the Zr-MOFs was examined by N_2 adsorption-desorption measurements at 77 K. All the PCN-160 derivatives show type I isotherms, confirming preserved microporosity. Pore size distributions calculated from the N_2 adsorption isotherms using a density functional theory (DFT) model fall in the range of 1.2–1.4 nm, comparable to that of pristine PCN-160 (1.4 nm). Variations in Brunauer-Emmett-Teller (BET) surface areas and pore size distributions arise from a combination of substituent steric effects and imine bond stability. Bulkier substituents (e.g., $–CH_3$ and –Cl) introduce greater steric hindrance within the pore channels, reducing accessible pore volume and BET surface areas. In contrast, smaller substituents (e.g., –H and –F) minimize steric obstruction and better preserve the intrinsic pore sizes (Figs. 2d, S20). In addition, substituent-dependent electronic effects influence imine bond stability, which can affect framework integrity during activation and further modulate BET surface area. For example, PCN-160-10 exhibits a lower BET surface area than expected due to partial framework decomposition during activation. Collectively, these results confirm the successful construction of a structurally consistent yet functionally diversified family of imine-linked PCN-160 frameworks, providing a suitable platform for tuning framework stability and dynamics.

Hammett-guided electronic regulation of framework dynamics

We first examined the electronic effects of functional groups on the intrinsic stability of imine-based linkers in solution. Formation and dissociation equilibrium constants of imine-linkers (L1-L10) were determined by ^{1}H NMR in the H_2O/dimethyl sulfoxide-d_6 (DMSO-d_6, 0.2%) solution (Figs. S21-30). To quantify the electronic effects of the substituents, we employed Hammett substituent constants (σ), which describe the electron-donating or electron-withdrawing ability of substituents relative to that of hydrogen[45–47]. Because the imine bond is inherently polarized ($C\delta^+ = N\delta^-$), substituents on the carbonyl-derived (C-side) and amine-derived (N-side) rings influence bond stability asymmetrically. To capture this electronic asymmetry, we define Δσ as the difference between the Hammett constants on the C-side and N-side aromatic rings ($\Delta\sigma = \sigma_C - \sigma_N$). Interestingly, a clear linear correlation between Δσ and the experimentally measured imine dissociation constants was observed (Fig. 3a), demonstrating that imine bond stability is governed by the electronic contrast between the two sides of the linkage. These results establish Hammett-guided electronic modulation as a predictive and quantitative handle for tuning imine bond stability, thereby providing a molecular foundation for regulating framework metastability upon incorporation into PCN-160.

We then evaluated how electronic effects of functional groups translate to MOF stability under aqueous conditions. After incubation in deionized water for 12 h, pronounced differences in PXRD peak intensities were observed across the PCN-160 series (Fig. 3b), revealing a clear stability hierarchy. PCN-160-X with electron-donating groups (e.g., –Me) on the N-side phenyl rings and electron-withdrawing substituents

(e.g., –F or –Cl) on the C-side phenyl rings (PCN-160-1 to PCN-160-6) exhibit high hydrolytic stability. In contrast, PCN-160-X derivatives bearing electron-withdrawing substituents (e.g., –F or –Cl) on the N-side phenyl rings (PCN-160-7 to PCN-160-10) rapidly lost crystallinity in aqueous environments.

To further differentiate the stability of the water-stable derivatives (PCN-160-1 to PCN-160-6), we evaluated their structural integrity across a broad pH range (Figs. 3d, S31-S33). PCN-160-1, with the largest Δσ, exhibited the largest pH stability window from 1 to 12. To more precisely define the stability limits of the water-unstable variants (PCN-160-7 to PCN-160-10), we exposed these materials to H_2O/DMSO mixtures with progressively increasing water content (Figs. 3c, S34-S35). This gradient experiment reveals a clear stability hierarchy, with structural integrity progressively decreasing from PCN-160-6 to PCN-160-10. The least stable derivative, PCN-160-10, underwent rapid structural collapse even at low water fractions in the H_2O/DMSO mixtures. Together, these results demonstrate that electronic substituent effects generate a continuum of framework stability, spanning from robust structures to over-destabilized variants prone to aqueous collapse.

Mechanistic elucidation of framework stability and dynamics

Although PCN-160-1 to PCN-160-9 display unchanged PXRD patterns after treatment in H_2O/DMSO, their imine bonds exhibit dynamic behavior to varying degrees. We first examined whether water exposure induces permanent compositional degradation within the stability window. TGA of samples treated with H_2O/DMSO (1:2 v/v) revealed that PCN-160-1 to PCN-160-9 retain thermal profiles consistent with their pristine structures, with no discernible evidence of defect formation or altered metal-to-ligand ratios (Fig. S36). Complementary inductively coupled plasma optical emission spectroscopy (ICP-OES) and high-performance liquid chromatography (HPLC) analyses further excluded significant metal or ligand leaching from these frameworks. These results indicate that, for derivatives within the stability window, aqueous exposure does not compromise the Zr–carboxylate backbone. This behavior is fundamentally distinct from conventional defect engineering in MOFs, where permanent removal of organic linkers or metal nodes creates static vacancies.

To elucidate the origin of instability at the extreme end of this stability spectrum, PCN-160-10 was selected as a representative case. After immersion in water for 12 h, the supernatant was analyzed by ICP-OES and HPLC to quantify metal and ligand release, respectively. No detectable Zr^{4+} leakage was observed, whereas ~ 7% ligand leaching was detected (Fig. S37), indicating that structural degradation originates from linker dissociation rather than metal leaching. The recovered solid after water treatment was subjected to TGA, N_2 adsorption, and Raman spectroscopy. TGA revealed a reduction in linker-to-metal ratio compared to the pristine materials (Fig. S38), consistent with the linker loss detected by HPLC. Meanwhile, Raman spectroscopy revealed the disappearance of imine bonds (Fig. 3g), and N_2 adsorption isotherms showed a dramatic loss of porosity (Fig. S39). These findings suggest that the excessive dynamics of the linkers trigger structural collapse, leading to the formation of amorphous products.

To probe the dynamic behavior of PCN-160-X derivatives, Raman spectroscopy was performed under different solvent conditions. Representative derivatives spanning the stability window (PCN-160-1, -3, -5, -7, and − 10) were selected for comparison. The characteristic C = N stretching band at ~ 1600 cm^{-1} serves as a diagnostic marker for imine integrity. Upon water treatment, stable derivatives (e.g., PCN-160-1) did not show any change in the C = N stretching band, whereas derivatives with intermediate stability (e.g., PCN-160-3 and PCN-160-5) exhibited slight attenuation of the C = N signal (Figs. 3e-f, S40), indicating partial imine dissociation. In contrast, water-unstable derivatives (PCN-160-7 and PCN-160-10) show a sharp C = N peak decrease, which is consistent with extensive bond cleavage (Figs. 3g, S41). Importantly, upon removal of water by washing with dry DMF, the imine bond signals for PCN-160-3 and 5 were fully restored to their initial intensities, whereas those of PCN-160-7 were only partially recovered. In contrast, no imine signal recovery was observed for totally collapsed PCN-160-10. These observations demonstrate that imine dissociation occurs in a substituent-dependent dynamic equilibrium, with reversibility preserved only within a defined metastable window. For derivatives within this metastable regime (e.g., PCN-160-3 and − 5), partial C = N bond cleavage does not disrupt the Zr–carboxylate backbone, enabling reversible C = N bond reformation upon removal of water. However, when the imine linkage becomes excessively labile (e.g., PCN-160-7 and − 10), bond cleavage propagates structural collapse, preventing reformation of the original imine bonds. In such cases, the dynamic equilibrium is lost, and bond dissociation becomes irreversible.

In vitro drug adsorption and release evaluation

To evaluate whether dynamic frameworks can accommodate guest molecules larger than their intrinsic apertures, the anticancer drug paclitaxel (PTX) was selected as a model cargo (Fig. 4a). As the molecular dimensions of PTX (20.9 × 13.5 × 11.2 Å) exceed the pore aperture of PCN-160 (~ 8 Å), its encapsulation requires transient aperture opening enabled by imine bond dissociation (Fig. S42). Drug loading was performed in a H_2O/DMSO mixture, where DMSO ensures the solubility of PTX and water promotes imine hydrolysis to activate framework dynamics. Optimization of the solvent composition identified a 1:2 (v/v) H_2O/DMSO ratio as optimal for maximizing PTX uptake (Fig. S43).

All the substituted PCN-160 derivatives exhibited measurable PTX loading with capacities strongly dependent on the substituents (Fig. 4b). Overly stable frameworks (e.g., pristine PCN-160) display limited linker dissociation and insufficient pore accessibility, excluding PTX from entering the pore. On the other hand, excessively unstable derivatives (e.g., PCN-160-10) undergo partial collapse, reducing effective porosity and cargo retention. An optimal balance between stability and dynamics is needed, with PCN-160-4 achieving a superior PTX uptake of 31.6 mg g^{-1}. Notably, PCN-160-4 retained a high BET surface area and pore volume even after aqueous incubation and PTX loading, as confirmed by N_2 adsorption measurements, demonstrating its preserved porosity (Fig. S44).

To further probe PTX adsorption and release kinetics, four materials spanning a representative range of framework stabilities (PCN-160-1, PCN-160-4, PCN-160-6, and PCN-160-10) were selected. All samples

exhibit rapid initial uptake (Fig. 4c), but differ markedly in their equilibrium capacities and adsorption profiles. These differences reflect the underlying stability of the frameworks. Highly stable PCN-160-1 limits dynamic aperture opening, whereas unstable PCN-160-10 suffers from pore blockage due to structural degradation, both resulting in reduced PTX uptake. To benchmark the performance of the PCN-160 series, microporous ZIF-8 was evaluated as a reference host material. Under identical conditions, rigid ZIF-8 exhibits negligible PTX adsorption, consistent with its small pore aperture (~ 3.4 Å), which prevents PTX from accessing the internal micropores.

The drug release profiles of PTX@PCN-160-1, -4, -6, and − 10 were evaluated in a phosphate-buffered saline (PBS) solution (pH 5.8), which mimics the tumor microenvironment. The observed substitent-dependent release kinetics show that PCN-160-4 exhibits optimal sustained-release behavior, achieving a drug release plateau (≥ 94% payload delivered) after 30 min (Fig. 4d). As a control, PTX@ZIF-8 was prepared through coprecipitation, which traps PTX during ZIF-8 growth. However, no drug release was observed within 30 minutes. The release behavior of PTX originates from water-induced imine hydrolysis and phosphate coordination to Zr clusters in PBS buffer solutions. These processes collectively promote extensive framework destabilization and decomposition, as evidenced by the disappearance of PXRD reflections and the attenuation of C = N signals in Raman spectra(Figs. S45-49). Thus, water-triggered imine dissociation combined with phosphate-induced coordination bond cleavage provides the mechanistic foundation for the observed drug release.

To validate the drug-loading versatility of PCN-160-4, other therapeutic agents (epirubicin and genistein) were tested (Figs. S50-51). Among them, epirubicin and genistein were effectively loaded, with the highest loading capacity observed for epirubicin at 60 mg g^{-1} (Fig. S52). These results highlight the versatility of PCN-160-4 as a drug delivery platform with high loading capacity and tunable release behavior. More broadly, the ability to modulate drug uptake and release through electronically programmed framework dynamics provides a general strategy for adapting delivery systems to diverse therapeutic requirements[48].

Cell apoptosis detection and cytotoxicity study

To further verify the practical application of PCN-160 in drug delivery, human breast cancer MCF-7 cells were employed (Fig. 5a). To assess the biocompatibility, MCF-7 cells (1×10^4 per well) were seeded in 6-well plates, cultured for 12 h, and then incubated with red fluorescent deoxyribonucleic acid (DNA)-labelled PCN-160-4 for 1 h. Confocal laser scanning microscopy (CLSM) revealed substantial intracellular MOF accumulation, as evidenced by the red fluorescence localized inside the green membrane boundaries (Fig. 5b). Cell apoptosis was subsequently analysed using an annexin V-fluorescein isothiocyanate (FITC)/propidium iodide (PI) assay. The externalization of phosphatidylserine, a result of early-stage apoptosis, was detected by annexin V—FITC protein staining, and membrane damage due to late-stage apoptosis was detected by the binding of PI to nuclear DNA[49]. After incubation with PCN-160-4 or PTX@PCN-160-4, apoptosis was evaluated by CLSM. As shown in Figs. 5c-d,

PTX@PCN-160-4 significantly induced apoptosis, whereas cells exposed to pure PCN-160-4 remained viable. Additionally, the inhibitory effects of the drug samples on cell growth were evaluated using a methylthiazolyldiphenyl-tetrazolium bromide (MTT) assay. After 24 h of exposure, > 95% of the viability was retained with PCN-160-4, whereas PTX@PCN-160-4 induced 87% apoptosis (Fig. 5e). Cytotoxicity assays of two additional agents revealed a limited MCF-7-killing capacity, with cell viability remaining > 60% (Fig. 5f). Together, these results demonstrate that electronically programmed framework dynamics enable efficient intracellular drug delivery while maintaining low carrier toxicity, highlighting the potential of this platform for controlled therapeutic applications.

Conclusions

In this work, we constructed a family of imine-linked MOFs with systematically varied substituents to modulate framework stability and dynamics. A quantitative correlation between Hammett parameters and imine dissociation equilibria demonstrates that electronic effects provide a predictive handle for regulating framework dynamics. Notably, this dynamic ligand strategy enables the accommodation of guest molecules larger than the intrinsic pore aperture of PCN-160-X, thereby resolving the critical size exclusion limitation inherent in conventional MOFs. As a proof of concept, we demonstrated efficient loading of anticancer drugs, followed by their controlled release in physiological environments, enabling effective delivery of water-insoluble drugs. Collectively, this work establishes the electronic modulation of dynamic covalent bonds as a rational design principle for programming framework dynamics, opening new opportunities for stimuli-responsive and size-adaptive porous materials.

Methods

Materials and Instrumentation.

All the reagents and solvents were commercially available and used without further purification. Deuterated solvents were purchased from Cambridge Isotope Laboratory (Andover, MA). ^{1}H NMR data were recorded on a Bruker Avance III 400 NMR spectrometer. ^{13}C NMR data were recorded on a Bruker Avance Neo 400 M spectrometer. Powder X-ray diffraction (PXRD) patterns were obtained at room temperature using a scan speed of 1 s/step on a Bruker Advance D8 (40 kV, 40 mA) diffractometer equipped with Cu radiation. FT-IR spectra were recorded on a Vector 27 Bruker Spectrophotometer by transmission through KBr pellets containing ground crystals in the range of 4000 – 400 cm^{-1}. Gas adsorption/desorption isotherms were measured using a Micrometritics ASAP 2020 system, PhysiChem iPore 620 Automated Surface Area and Micropore Analyzer, and a BSD-PS4 gas adsorption analyzer. TGA data were obtained on a TGA 4000 thermal analysis system at a heating rate of 10°C·min^{-1} under an air atmosphere. Simulated PXRD patterns were generated from single-crystal data using Mercury 3.0. The morphology and elemental mapping of the samples were characterized by field emission scanning electron microscopy (SEM; Quanta 250F). Confocal laser microscopy (CLSM) images were obtained with a Nikon AX with excitation wavelengths of 488 nm and 561 nm.

Synthesis of PCN-160 (large crystals).

$ZrCl_4$ (200 mg), H_2AZDC (100 mg), trifluoroacetic acid (1.3 mL), and DMF (18 mL) were charged in a Pyrex vial. The mixture was heated in a 120°C oven for 72 h. After cooling to room temperature, the red crystals were harvested.

Synthesis of PCN-160 (nanocrystals).

$ZrCl_4$ (23.4 mg), H_2AZDC (27 mg), glacial acetic acid (172 μL), and DMF (5 mL) were added to a 15 mL Teflon-lined stainless-steel autoclave and sonicated for 5 min. The sealed vessel was then heated at 100°C under stirring for 12 h. The resulting orange precipitate was separated by centrifugation at 8000 rpm for 5 min and washed several times with DMF to yield the product.

Synthesis of PCN-160-X.

PCN-160-X (X = 1–10) was synthesized via complete linker exchange of AZDC in PCN-160 with the corresponding solutions (as detailed in Tab. S1). Typically, crystals of PCN-160 were incubated with these solutions at 75°C. Linker exchange was performed by repeatedly replacing the supernatant with fresh stock solution every 5 h until the color of the supernatant closely matched that of the exchange solution.

Declarations

Author Contributions Statement

M.Q. and Y.C.L. contributed equally to this work. S.Y. and X.Z. conceived the original idea. M.Q. and Y.C.L. performed the synthesis. M.Q. and Y.C.L. performed the comprehensive structural characterization, property measurements, and data analysis. S.C.C. tested drug adsorption and release. S.R.L performed the MTT assay. Y.H.G. and D.Z. performed crystal analysis. Y.F.L. conducted the Raman measurements. L.G. and M.T.C. conducted the Δσ and molecular size calculations. M.Q., Y.C.L., S.Y., and X.Z. drafted the manuscript. All the authors contributed to the revision of the manuscript.

Additional information

Supplementary information is available in the online version of the paper.

Reprints and permissions information are available online at www.nature.com/reprints.

Correspondence and requests for materials should be addressed to X.Z. or S.Y.

Competing financial interests

The authors declare that they have no competing financial interests.

Acknowledgments

This work was supported by the Jiangsu Basic Research Center for Synthetic Biology Grant (No.BK20233003; X.Z.), the National Key Research and Development Program of China (2025YFA1511500; 2024YFA1510301; S.Y.), the National Natural Science Foundation of China (223B2107, 22271141, T2541071; S.Y., Y.C.L.), the Natural Science Foundation of Jiangsu Province (BK20250064; S.Y.), and the Jiangsu Province Natural Science Funds for Distinguished Young Scholars (BK20240032; X.Z.).

Data availability

The X-ray crystallographic data for structures reported in this article have been deposited at the Cambridge Crystallographic Data Centre (CCDC), under deposition numbers CCDC 2538814 and 2538822 (Tabs. S2-4), for compounds PCN-160-1 to PCN-160-10, respectively, which can be obtained from the CCDC via https://www.ccdc.cam.ac.uk/structures/. All other data that support the results in this study are available from the corresponding author upon reasonable request.

References

1. Furukawa H, Cordova KE, O'Keeffe M, Yaghi OM (2013) The chemistry and applications of metal-organic frameworks. Science 341:1230444
2. Horike S, Kitagawa S (2022) The development of molecule-based porous material families and their future prospects. Nat Mater 21:983–985
3. Yaghi OM (2016) Reticular chemistry—construction, properties, and precision reactions of frameworks. J Am Chem Soc 138:15507–15509
4. Kitagawa S, Kitaura R, Noro S (2004) Functional porous coordination polymers. Angew Chem Int Ed 43:2334–2375
5. Ji Z, Wang H, Canossa S, Wuttke S, Yaghi OM (2020) Pore chemistry of metal–organic frameworks. Adv Funct Mater 30:2000238
6. Wuttke S (2025) Toward the nobel prize: dissecting fundamental principles and applications of MOF and COF materials. Adv Mater 37:e71859
7. Chen Z, Kirlikovali KO, Li P, Farha OK (2022) Reticular chemistry for highly porous metal–organic frameworks: the chemistry and applications. Acc Chem Res 55:579–591
8. Robison L et al (2021) Transient catenation in a zirconium-based metal–organic framework and its effect on mechanical stability and sorption properties. J Am Chem Soc 143:1503–1512
9. Lyu H et al (2022) Carbon dioxide capture chemistry of amino acid functionalized metal–organic frameworks in humid flue gas. J Am Chem Soc 144:2387–2396
10. Chen OI-F et al (2024) Water-enhanced direct air capture of carbon dioxide in metal–organic frameworks. J Am Chem Soc 146:2835–2844

11. Foo ML et al (2016) An adsorbate discriminatory gate effect in a flexible porous coordination polymer for selective adsorption of CO_2 over C_2H_2. J Am Chem Soc 138:3022–3030
12. Fracaroli AM et al (2014) Metal–organic frameworks with precisely designed interior for carbon dioxide capture in the presence of water. J Am Chem Soc 136:8863–8866
13. He D et al (2024) Self-assembly of chiral porous metal–organic polyhedra from trianglsalen macrocycles. J Am Chem Soc 146:17438–17445
14. Liao P-Q, Huang N-Y, Zhang W-X, Zhang J-P, Chen X-M (2017) Controlling guest conformation for efficient purification of butadiene. Science 356:1193–1196
15. Rieth AJ, Wright AM, Dincă M (2019) Kinetic stability of metal–organic frameworks for corrosive and coordinating gas capture. Nat Rev Mater 4:708–725
16. Melle F et al (2025) Rational design of metal–organic frameworks for pancreatic cancer therapy: from machine learning screening to In vivo efficacy. Adv Mater 37:2412757
17. He C, Liu D, Lin W (2015) Nanomedicine applications of hybrid nanomaterials built from metal–ligand coordination bonds: nanoscale metal–organic frameworks and nanoscale coordination polymers. Chem Rev 115:11079–11108
18. Yu Z et al (2025) MOF-enhanced phototherapeutic wound dressings against drug-resistant bacteria. Adv Healthc Mater 14:2402418
19. Simon-Yarza T, Mielcarek A, Couvreur P, Serre C (2018) Nanoparticles of metal-organic frameworks: on the road to In vivo efficacy in biomedicine. Adv Mater 30:1707365
20. Ma X et al (2025) An engineered iron-based MOF for siRNA delivery targeting chemotherapy-resistant triple-negative breast cancer. *ChemRxiv* (2025)
21. Chen Y et al (2025) Tetrazine-enhanced donor-acceptor-donor metal-organic frameworks for photodynamic antibacterial therapy and wound healing. Nat Commun 16:10508
22. Li Z et al (2025) Advances in biocompatible metal-organic frameworks for biomedical applications. Adv Mater 37:2503946
23. Huang S, Chen G, Ouyang G (2022) Confining enzymes in porous organic frameworks: from synthetic strategy and characterization to healthcare applications. Chem Soc Rev 51:6824–6863
24. Wang K-Y et al (2023) Bioinspired framework catalysts: from enzyme immobilization to biomimetic catalysis. Chem Rev 123:5347–5420
25. Liang K et al (2015) Biomimetic mineralization of metal-organic frameworks as protective coatings for biomacromolecules. Nat Commun 6:7240
26. Abánades Lázaro I, Wells CJR, Forgan RS (2020) Multivariate modulation of the Zr MOF UiO-66 for defect-controlled combination anticancer drug delivery. Angew Chem Int Ed 59:5211–5217
27. Zheng H et al (2016) One-pot synthesis of metal–organic frameworks with encapsulated target molecules and their applications for controlled drug delivery. J Am Chem Soc 138:962–968
28. Deng H et al (2012) Large-pore apertures in a series of metal-organic frameworks. Science 336:1018–1023

29. Morabito JV et al (2014) Molecular encapsulation beyond the aperture size limit through dissociative linker exchange in metal–organic framework crystals. J Am Chem Soc 136:12540–12543
30. Feng Y et al (2023) A dynamic defect generation strategy for efficient enzyme immobilization in robust metal-organic frameworks for catalytic hydrolysis and chiral resolution. Angew Chem Int Ed 62:e202302436
31. Cohen SM (2017) The postsynthetic renaissance in porous solids. J Am Chem Soc 139:2855–2863
32. Cohen SM (2012) Postsynthetic methods for the functionalization of metal–organic frameworks. Chem Rev 112:970–1000
33. Vermoortele F et al (2013) Synthesis modulation as a tool to increase the catalytic activity of metal–organic frameworks: the unique case of UiO-66(Zr). J Am Chem Soc 135:11465–11468
34. Yuan S et al (2017) Construction of hierarchically porous metal–organic frameworks through linker labilization. Nat Commun 8:15356
35. Feng L et al (2018) Creating hierarchical pores by controlled linker thermolysis in multivariate metal–organic frameworks. J Am Chem Soc 140:2363–2372
36. Guillerm V, Xu H, Albalad J, Imaz I, Maspoch D (2018) Postsynthetic selective ligand cleavage by solid–gas phase ozonolysis fuses micropores into mesopores in metal–organic frameworks. J Am Chem Soc 140:15022–15030
37. Qiao M et al (2024) Unlocking of hidden mesopores for enzyme encapsulation by dynamic linkers in stable metal-organic frameworks. Angew Chem Int Ed 63:e202409951
38. Deng H, Olson MA, Stoddart JF, Yaghi OM (2010) Robust dynamics. Nat Chem 2:439–443
39. Brozek CK et al (2015) Dynamic DMF binding in MOF-5 enables the formation of metastable cobalt-substituted MOF-5 analogues. ACS Cent Sci 1:252–260
40. Henke S, Schneemann A, Wütscher A, Fischer RA (2012) Directing the breathing behavior of pillared-layered metal–organic frameworks via a systematic library of functionalized linkers bearing flexible substituents. J Am Chem Soc 134:9464–9474
41. Li Z, Rayder TM, Luo L, Byers JA, Tsung C-K (2018) Aperture-opening encapsulation of a transition metal catalyst in a metal–organic framework for CO_2 hydrogenation. J Am Chem Soc 140:8082–8085
42. Li Y et al (2026) Dynamic bond-driven encapsulation of enzymes in metal–organic frameworks beyond pore size constraints. Nat Commun. https://doi.org/10.1038/s41467-026-70249-x
43. Qiao S et al (2026) Dynamic exchange assembly of enzymes with single-crystal covalent organic frameworks. *J. Am. Chem. Soc.* jacs.5c22300 10.1021/jacs.5c22300
44. Yuan S et al (2018) Exposed equatorial positions of metal centers via sequential ligand elimination and installation in MOFs. J Am Chem Soc 140:10814–10819
45. Jaffé HH (1953) A reëxamination of the hammett equation. Chem Rev 53:191–261

46. Hammett LP (1935) Some relations between reaction rates and equilibrium constants. Chem Rev 17:125–136
47. Lewis GN (1916) The atom and the molecule. J Am Chem Soc 38:1–24
48. Tibbitt MW, Dahlman JE, Langer R (2016) Emerging frontiers in drug delivery. J Am Chem Soc 138:704–717
49. Kumar R, Saneja A, Panda AK (2021) An annexin V-FITC—propidium iodide-based method for detecting apoptosis in a non-small cell lung cancer cell line. In: Santiago-Cardona PG (ed) Lung Cancer: Methods and Protocols. Springer US, New York, NY, pp 213–223. doi:10.1007/978-1-0716-1278-1_17.

Figures

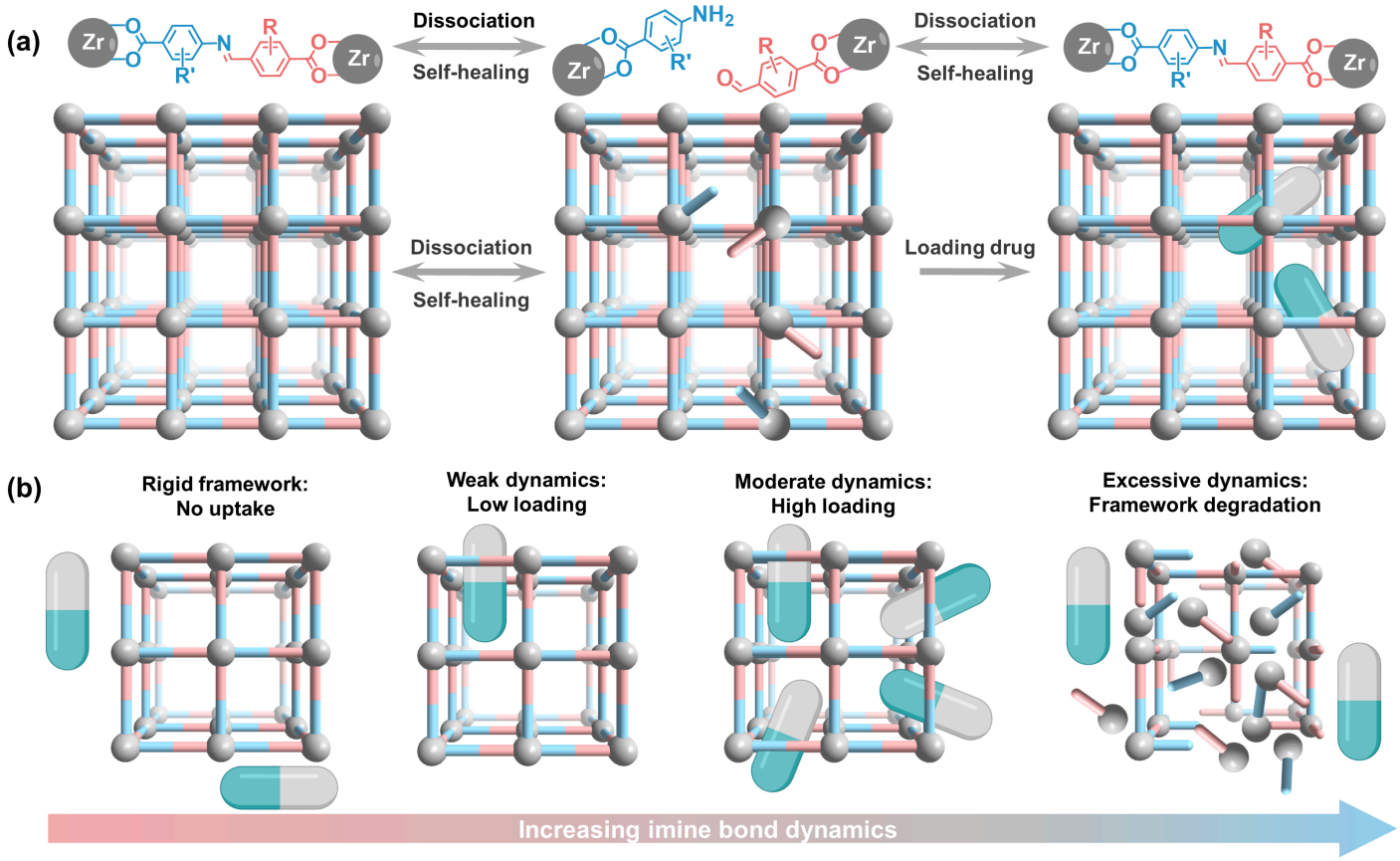

Figure 1

Dynamic imine bonds enable programmable pore gating and enhanced guest uptake in MOFs. (**a**) Schematic illustration of dynamic imine bond dissociation and reformation, which transiently opens pore apertures and enables the encapsulation of guest molecules larger than the intrinsic pore windows. (**b**) Impact of framework dynamics on guest loading behavior.

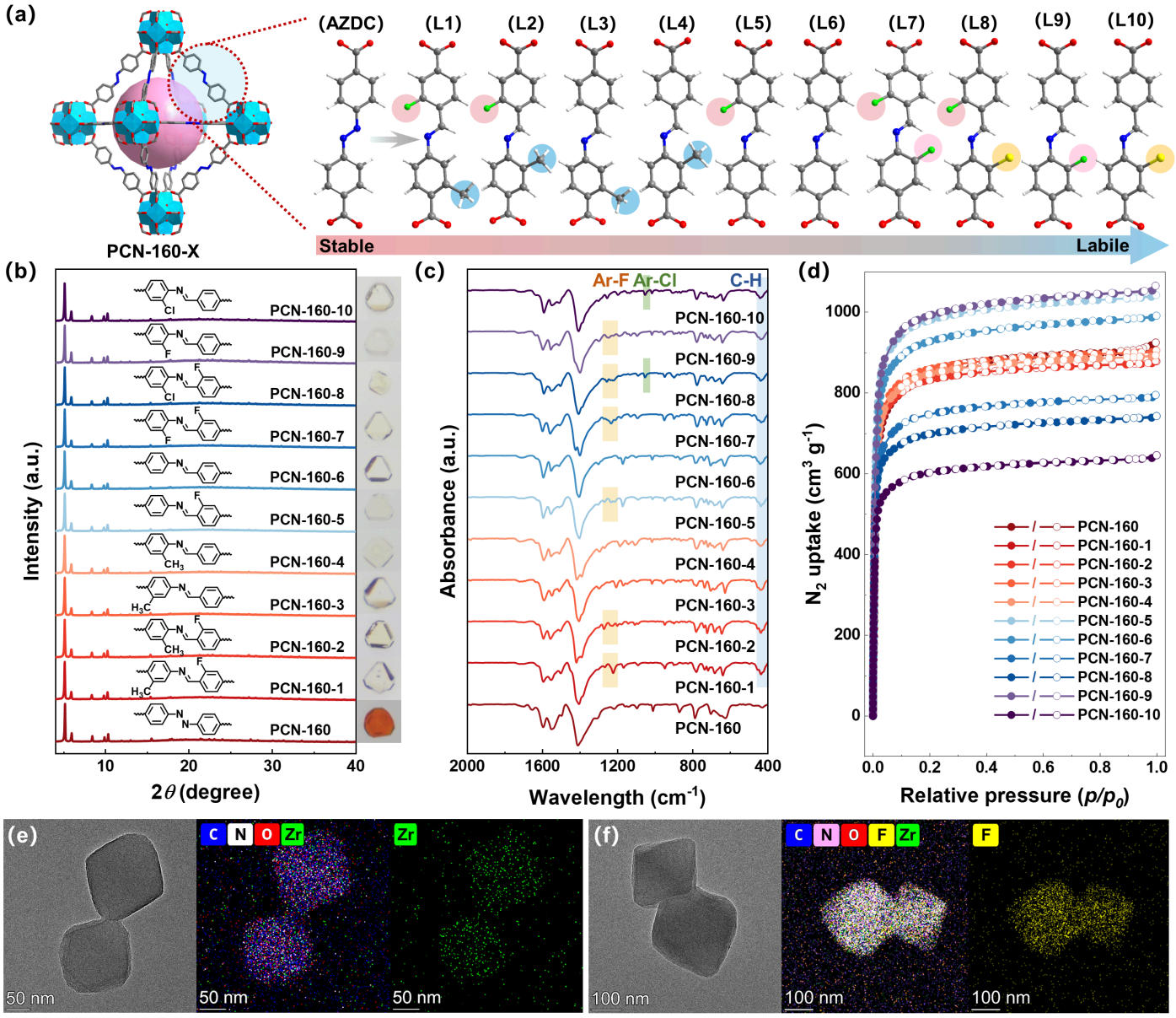

Figure 2

Structural characterization of imine-based PCN-160-X (X = 1-10). (**a**) Single crystal structure of PCN-160-X with imine linker substituent highlighted. PXRD (**b**), IR spectra (**c**), and N_2 absorption (**d**) of PCN-160-X. Inset show photographs of PCN-160-X single crystals. (**e,f**) TEM images and corresponding elemental mapping of pristine PCN-160 and PCN-160-2, showing preserved morphology and uniform elemental distribution.

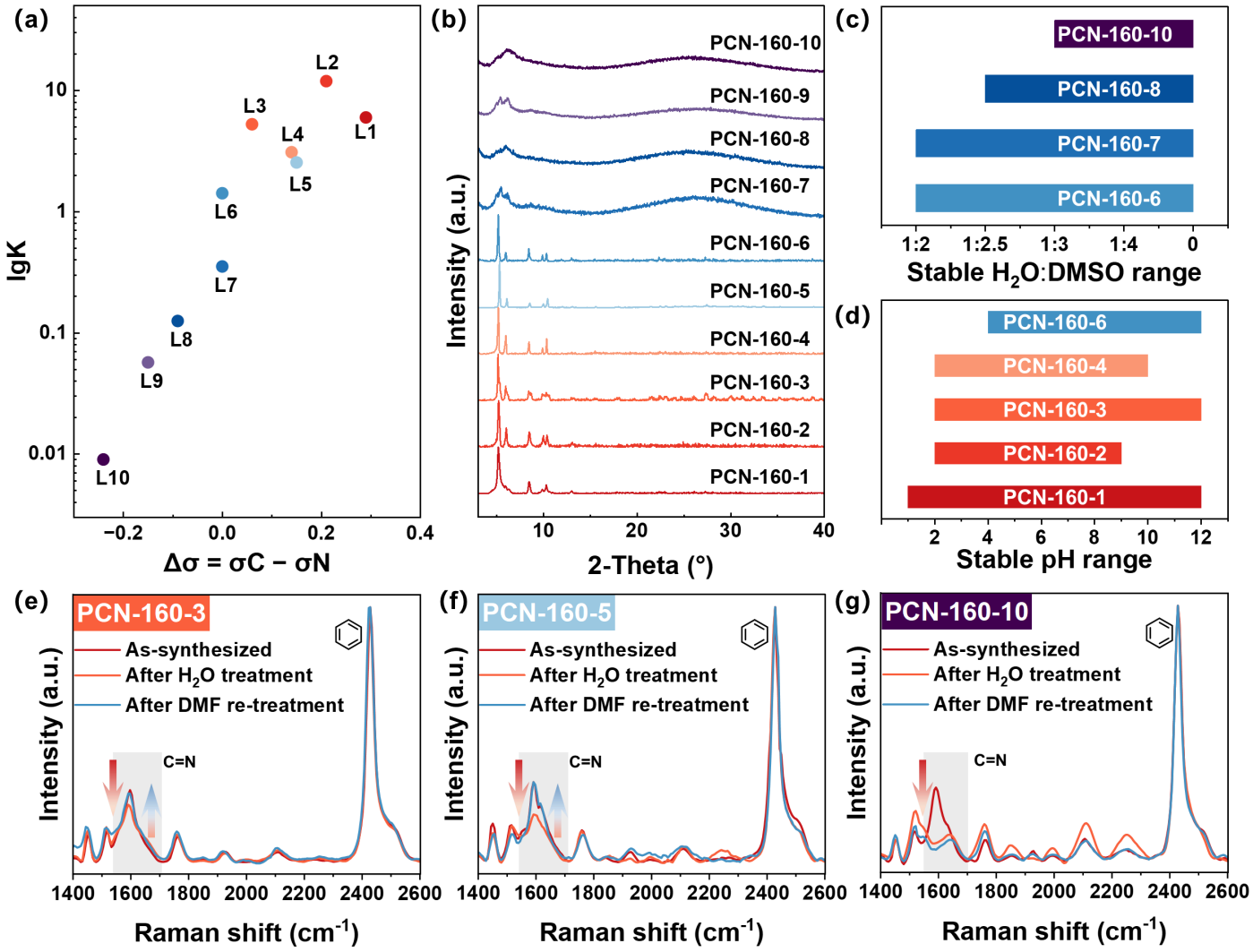

Figure 3

Electronic tuning of imine bond dynamics and framework stability in PCN-160-X. (**a**) Correlation between imine equilibrium constants (log K) and electronic parameter Δσ. (**b**) PXRD patterns of PCN-160-X (X = 1–10) after immersion in water for 12 h, showing substituent-dependent stability. Stability of selected PCN-160 derivatives under varying pH conditions in water (**c**) and different water concentration in H_2O/DMSO mixtures (**d**), as evaluated by PXRD. Raman spectra of PCN-160-3 (**e**), PCN-160-7 (**f**) and PCN-160-10 (**g**) under different conditions (as-synthesized in DMF, after water immersion, and redissolved in DMF), revealing reversible and irreversible imine bond behavior.

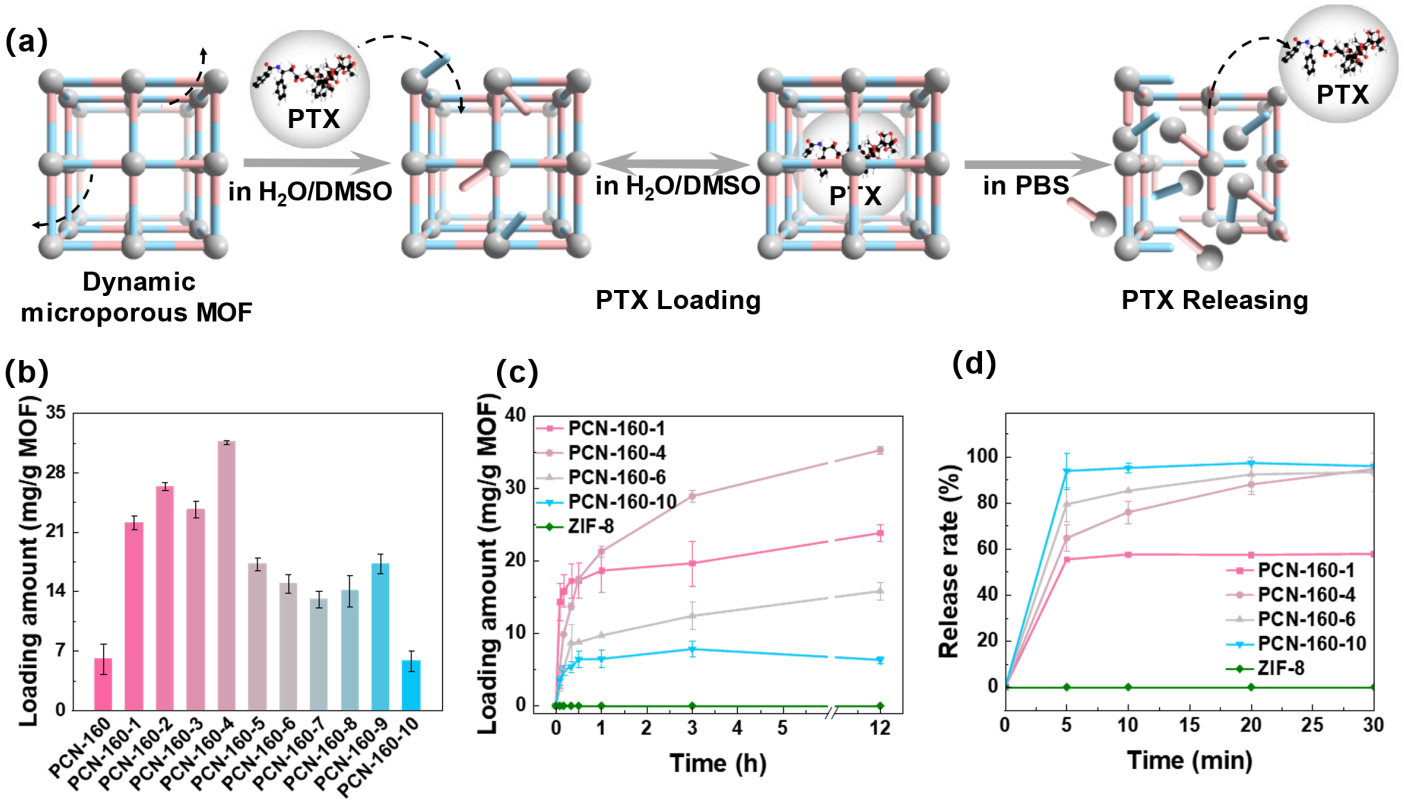

Figure 4

Dynamic MOF-mediated paclitaxel loading and release. (**a**) Schematic illustration of PTX encapsulation via dynamic imine bond dissociation in H_2O/DMSO and release in PBS. (**b**) PTX adsorption capacity of PCN-160-X (X = 1-10) after 12 h. Time-dependent profiles of PTX adsorption (**c**) and release (**d**) by the dynamic PCN-160-1, -4, -6, and -10.

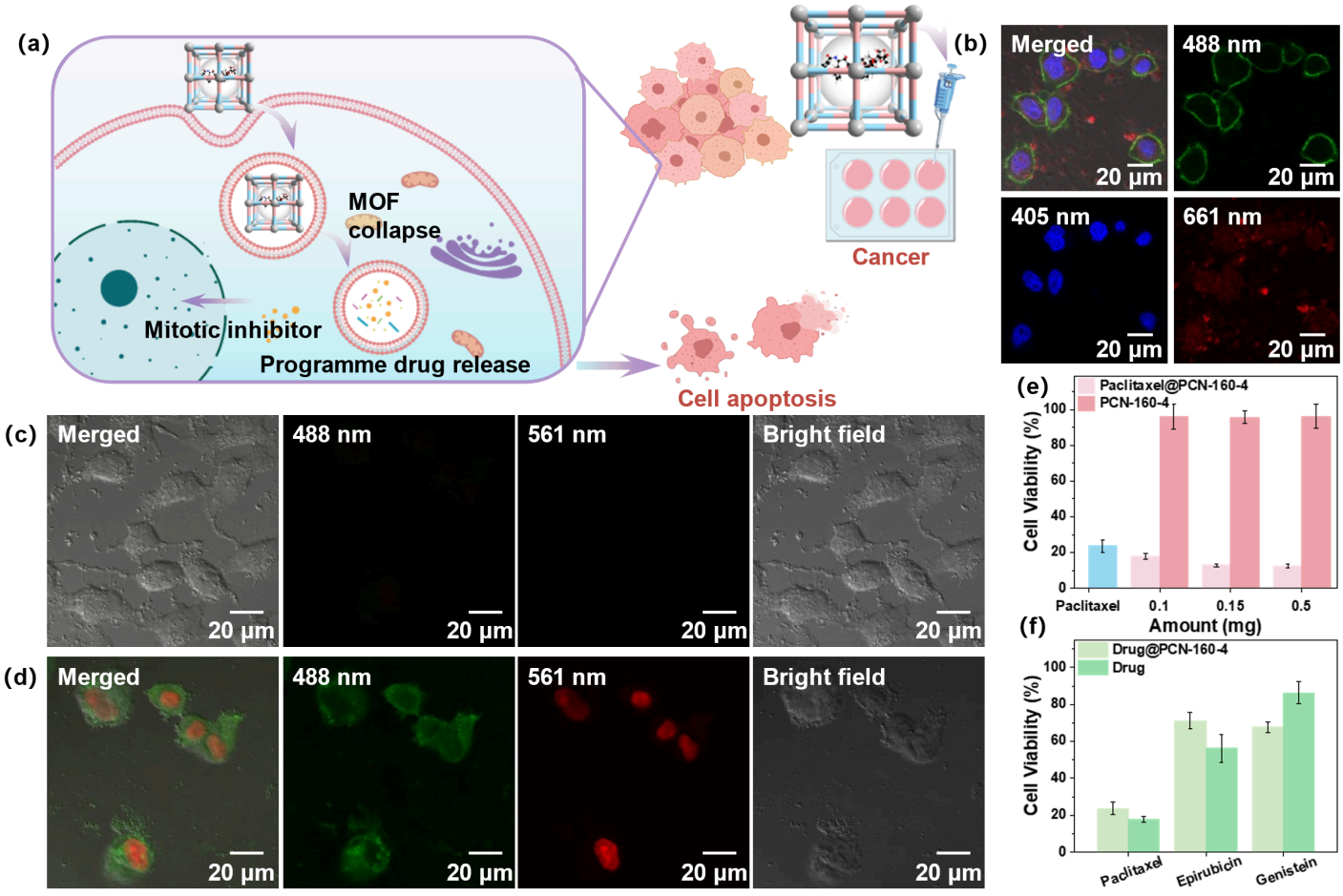

Figure 5

Cellular internalization and anticancer efficacy of PTX@MOF. (**a**) Schematic illustration of PTX@MOF cellular entry via endocytosis and subsequent cancer apoptosis. (**b**) CLSM images confirming the cellular internalization of PCN-160-4 (red). Nuclei and cell membranes are stained blue and green, respectively. Apoptosis assay of PCN-160-4 (**c**) and PTX@PCN-160-4 (**d**) detected by an annexin V-FITC/PI assay kit; apoptotic cells are dually stained red and green. (**e**) Cytotoxicity evaluation of PCN-160-4 against MCF-7 cells. (**f**) Comparative cytotoxicity of free drugs and the drug@MOF formulation on MCF-7 cells.

Supplementary Files

This is a list of supplementary files associated with this preprint. Click to download.

- SupplementaryInformation.pdf